Available online at www.sciencedirect.com
SCIENCE DIRECT®
Journal of Computational Physics 210 (2005) 55–74
JOURNAL OF COMPUTATIONAL PHYSICS
www.elsevier.com/locate/jcp

Sharp interface Cartesian grid method III: Solidification of pure materials and binary solutions

Yi Yang, H.S. Udaykumar *

Department of Mechanical and Industrial Engineering, University of Iowa, 3026 Seamans Center, Iowa City, IA 52242, United States

Received 30 June 2004; received in revised form 4 April 2005; accepted 14 April 2005
Available online 7 July 2005

Abstract

A numerical technique is presented for computing dendritic growth of crystals from pure melts and binary solutions. The governing equations are solved on a fixed Cartesian mesh and the immersed phase boundary is treated as a *sharp* solid–fluid interface. The interface is tracked using a level-set field. A finite-difference scheme is presented that incorporates the immersed phase boundary with only a small change to a standard Cartesian grid Poisson solver. The scheme is simple to implement in three-dimensions. The results from our calculations show excellent agreement with two-dimensional microscopic solvability theory for pure material solidification. It is shown that the method predicts dendrite tip characteristics in excellent agreement with the theory. The sharp interface treatment allows discontinuous material property variation at the solid–liquid interface. This facilitates sharp-interface simulations of dendritic solidification of binary solutions.

Keywords: Sharp interface methods; Levelsets; Dendritic growth; Alloys

1. Introduction

In previous work [1] a finite-difference technique was developed for the simulation of diffusion-controlled growth of unstable phase boundaries. For the case of dendritic solidification of pure materials from the melt, it was demonstrated that a *sharp interface* approach can be developed that yields globally second-order accurate solutions to the field equations. The interface position was computed with first-order accuracy. In subsequent work [2,3], a finite-volume approach was devised for solving

DOI of original article: 10.1016/j.jcp.2005.03.031, 10.1016/j.jcp.2005.03.032.
* Corresponding author. Tel.: +1 319 384 0832; fax: +1 319 335 5669.
E-mail address: ush@icaen.uiowa.edu (H.S. Udaykumar).

0021-9991/$ - see front matter
doi:10.1016/j.jcp.2005.04.024

the incompressible Navier–Stokes equations to compute flows around fixed and moving immersed solid bodies. While the finite-volume scheme is strictly conservative in its construction because the weak form of the equations is solved with explicit enforcement of flux continuity on contiguous control volume faces, extension of the technique to three-dimensions is challenging. In Part I [4] it was shown that it is possible to obtain a finite-difference scheme, in the spirit of the ghost fluid method [5] and immersed interface method [6,7], that yields second-order accurate solutions in the presence of embedded interfaces. The results were shown to be identical to the more complicated finite volume technique.

This paper applies the basic framework laid out in [4] and demonstrates that a finite-difference method can be constructed with considerable simplicity, while computing phase change phenomena in the strict sharp interface limit. The technique is applied to study dendritic growth in both pure and impure melts. The present work places the scheme on sound footing by directly comparing the results of the computations with two-dimensional microscopic solvability theory for solidification of pure materials. The method is shown to predict the correct physical behavior in the dendritic growth of impure materials.

2. Sharp versus diffuse interface methods for solidification

Several techniques are now available for the simulation of solidification microstructures, particularly dendritic structures that are predominant in the bulk of solidified metallic materials. Approaches based on phase-fields [8–11], level-sets [12–15], finite-elements [16–19], finite-difference front-tracking [1,20–22], and cellular automata [23,24] have been employed to simulate this pattern-forming phenomenon. These methods can be broadly classified into two categories, viz., *diffuse* and *sharp* interface methods.

From a mathematical model standpoint, diffuse interface methods [25] transmit the effects of the interface to the temperature and species field equation solver through source terms in the transport equations, viz.:

$$\beta_t \frac{\partial \xi}{\partial t} + \vec{\nabla} \cdot (\vec{u}\xi) = \nabla \cdot \beta_d (\nabla \xi) + S(\vec{x}, t). \tag{1}$$

The source term $S(\vec{x}, t)$ may represent the effects of latent heat release, solute partition, capillarity and other interfacial effects. Typically, through the source term $S(\vec{x}, t)$, the temperature and species fields couple to the evolution of an order parameter that distinguishes the phases present. In this category, the phase-field method is currently the most popular and was the first approach used [26–28] to determine whether the quantitative measures, such as tip radius, velocity and the selection parameter of numerically grown dendrites could be validated against microscopic solvability theory [29,30]. By construction, in diffuse interface methods the interface is not a sharp phase boundary but is given a certain thickness or spread on the computational mesh. Typically, the interface thickness occupies a few mesh spacings. Thus, both delta (singular sources residing on the interfaces, such as latent heat and capillarity) and Heaviside (such as jump discontinuities in material properties) functions are replaced by smoothed numerical approximations. Diffuse interface methods, particularly the phase-field method, have been applied extensively for a wide variety of problems in solidification to date [10,26]. Improvements to the method to improve speed and efficiency have also been proposed [31–35]. The work of Juric and Tryggvason [22] and more recently Al-Rawahi and Tryggvason [20,21] may be considered to be a hybrid method because although the interface is tracked sharply as a curve in 2D (surface in 3D), the effect of the interface is transmitted to the field equation solver using smoothed delta and Heaviside functions in the spirit of the immersed boundary method [36].

Sharp interface methods do not employ a source term in the governing equation. In such methods, during the discretization procedure the spatial differential operators $(\vec{\nabla}, \nabla^2)$ in the equation are constructed at points that adjoin the interface in such a way that the interfacial jump conditions are incorporated.

Examples of this class are the immersed interface method [7,37,38], the sharp interface method [2,39,40], the ghost fluid method [5,41] and the XFEM method [42–45].

Comparison of a sharp interface method with solvability theory in two-dimensions was performed by Dantzig and co-workers [15]. They used a level-set technique for tracking the front and a finite-element method for solution of the diffusion equation. The idea of using level-sets along with a finite-difference solution of the diffusion equations with application to phase change was also used in the work of [12,14,13,46]. Three-dimensional results as well as fourth-order discretization using a ghost fluid approach for the Poisson equation were shown in the latter papers. Finite element methods have been used to perform sharp interface calculations with various approaches to interface tracking and solution of the field equations. Schmidt [17] used boundary conforming unstructured finite element meshes including remeshing and local refinement in what can be considered to be a classic sharp interface approach. In a similar vein, Jaeger and Carin [47] have solved the problem of solidification of aqueous solutions using a method that tracks the interface explicitly as curves on an unstructured mesh and remeshes near the interface so that the mesh conforms locally to the interface. Zhao and co-workers [18,19] also follow the interface evolution using curve tracking but solve the field equation using a finite-element solver by reconfiguring the interface-containing elements. The X-FEM [43] approach involves tracking the interface using level-sets and redefining (i.e. enriching), the elements through which the interface passes. Remeshing is not performed here but enrichment involves redefining the interface-containing element for integration of the weak form. Pure material solidification has been solved using this approach. Udaykumar and co-workers [2] used a finite-volume method and explicit front-tracking to compute the evolution of sharp dendritic fronts, in pure materials [48], solutions [49], in the presence of particles such as biological cells [50] and ceramic reinforcements [51,52] and in the presence of fluid flow [48]. The results were shown to match very well with solvability theory for dendrites in a pure material and exact solutions and numerical benchmarks in other cases.

Typically, diffuse interface methods have been assumed to be simpler to implement, particularly in multi-dimensions, and to more easily handle topological changes and therefore have found wide usage [10,25]. However in such method care is demanded in formulating the governing equation so that the sharp interface limit can be recovered in the limit of vanishing interface thickness. Sharp interface methods rely on straightforward field equations and interface balance conditions but have been considered to be somewhat more difficult to implement; therefore their use has been restricted to some specific situations and to a few practitioners. The present paper and the companion papers [4,53] seek to demonstrate that sharp interface methods can be developed and implemented with considerable ease and applied to a variety of moving boundary problems. It has been shown that going from two to three dimensions can also be accomplished fairly easily with the framework presented in this paper [4]. With a level-set interface representation topological changes present no difficulties.

3. The current method

As pointed out before, the framework of a level-set method combined with the finite-difference solver for phase change calculations is not new. This has been used by other researchers [12–15] with some differences from the present paper. However, this paper distinguishes itself from these earlier efforts in the following respects:

1. The scheme is presented in a simple-to-implement formulation that will involve the addition of only a modest amount of code to a standard Cartesian grid solver. Global second-order accuracy is maintained.
2. The computation of dendritic solidification of binary mixtures is demonstrated for the first time in this framework. This requires some care and additional algorithmic rearrangements over the pure material case.

3. The interface velocity has to be computed with care and the procedures for obtaining second-order accurate interface velocities are described.
4. Analysis to obtain an a priori estimate of the grid required for obtaining grid-independent sharp-interface solutions is performed. In the past, these requirements have been established on a case-by-case basis and by a cut-and-try approach. An attempt is made to correlate the grid independence conditions with the parameters that control the steady shape of the growing dendrite.

Although we have restricted computations in the present paper to two-dimensional cases, the methods laid out in the following are easily extended to three-dimensions as demonstrated for other moving boundary problems in [4].

4. Formulation for solidification of pure and impure materials

4.1. Governing equations

The governing equations for diffusive heat and solute transport are non-dimensionalized by choosing the following scales (defined separately for each of the cases shown in the results section): length scale = X a characteristic length for the system, time scale $= \frac{X^2}{\eta_L}$, where η_L is a characteristic diffusion coefficient, velocity scale $= \frac{\eta_L}{X}$ concentration scale = c_0, the initial solute concentration, temperature scale = T_S. The non-dimensional temperature is defined to be $\Theta = (T - T_m)/T_S$, where T_m is the melting point of the pure substance (or solvent) and non-dimensional concentration $c = C/c_0$, where c_0 is the concentration of solute in the initial solution. The non-dimensionalized equations are then written as follows:

Energy equation:

$$\frac{\partial \Theta}{\partial t} = \alpha^*_{L/S} \nabla^2 \Theta, \tag{2}$$

where $\alpha^*_{L/S}$ is the non-dimensional thermal diffusion coefficient in the liquid/solid phase.

Species equation in the solid:

$$\frac{\partial c_S}{\partial t} = D^*_S \nabla^2 c_S \tag{3}$$

and species diffusion in the liquid:

$$\frac{\partial c_L}{\partial t} = D^*_L \nabla^2 c_L, \tag{4}$$

$D^*_{L/S}$ is the non-dimensional species diffusion coefficient in the liquid/solid phase.

The interface conditions become, in non-dimensional form:

$$V_N = \frac{k_L \cdot T_S}{H_{SL} \cdot \eta_L} \cdot \left[\frac{k_S}{k_L} \cdot \left(\frac{\partial \Theta}{\partial n} \right)_S - \left(\frac{\partial \Theta}{\partial n} \right)_L \right], \tag{5}$$

where k_L is the thermal conductivity, H_{SL} is the latent heat per unit volume. We define a Stefan number, $St = \frac{k_L \cdot T_S}{H_{SL} \cdot \eta_L}$.

$$V_N = \frac{D^*_L}{(1-k) \cdot c_{Ll}} \cdot \left[\frac{D_S}{D_L} \cdot \left(\frac{\partial c}{\partial n} \right)_S - \left(\frac{\partial c}{\partial n} \right)_L \right] \tag{6}$$

and

$$\Theta_{\mathrm{L,int}} = \frac{b_1 \cdot c_0}{T_{\mathrm{S}}} \cdot c_{\mathrm{L}I} + \frac{b_2 \cdot c_0^2}{T_{\mathrm{S}}} c_{\mathrm{L}I}^2 + \frac{b_3 \cdot c_0^3}{T_{\mathrm{S}}} c_{\mathrm{L}I}^3 + \frac{b_4 \cdot c_0^4}{T_{\mathrm{S}}} c_{\mathrm{L}I}^4 - \Gamma(\theta)\kappa^*, \tag{7}$$

where

$$\Gamma(\theta) = \frac{\gamma_0 T_{\mathrm{m}}}{H_{\mathrm{SL}} X T_{\mathrm{S}}} (1 - 15\varepsilon \cos(m(\theta - \theta_0))) \tag{8}$$

is the non-dimensional capillarity parameter. $\Gamma_0 = \frac{\gamma_0 T_{\mathrm{m}}}{H_{\mathrm{SL}} T_{\mathrm{S}}}$ is a capillary length.

The values of the constants b_0 to b_4 are given in the results section for the particular solution (NaCl–H_2O) chosen here for the numerical calculations (corresponding to data in [54]). Note that the interfacial tension has a directional dependency, which reflects crystalline anisotropy [15,28].

4.2. A general form of the discretization for the operators

The transport equations for scalar (heat and species) transport are discretized as follows:

$$\beta_{\mathrm{t}} \frac{\xi^n + 1}{\Delta t} - \frac{\beta_{\mathrm{d}}}{2}[\nabla^2 \xi^n + 1] = \beta_t \frac{\xi^n}{\Delta t} + \frac{\beta_{\mathrm{d}}}{2}[\nabla^2 \xi^n], \tag{9}$$

where β_{t} and β_{d} are coefficients accompanying the time-dependent and diffusive parts of the equations. The diffusion term has been discretized in time using the second-order accurate Crank–Nicolson scheme.

The phase boundary can cut through the mesh in an arbitrary fashion leading to several different configurations of interfacial nodes. Some situations are illustrated in Fig. 1(a). The central idea here is that the discretization procedures can be generalized in a straightforward way for implementation purposes without concerning oneself with the details of the embedded geometry. This is facilitated by using the distance function information provided by the levelset field that defines the interface [4,53]. The Laplacian operator in the scalar diffusion equation can be discretized by considering derivatives along the coordinate directions and the final 3D discrete form assembled in a unified manner by using switch functions that depend on the signed distance function information [55]. The following expressions apply where multiple (say $L_{\max}$) embedded boundaries (represented and tracked as levelset functions $\phi_l(\vec{x}, t)$, $l = 1$ to $L_{\max}$) are present in the flow. For components along the x-direction the scheme is as follows:

Define a sign function:

$$\begin{aligned} (s_l)_{\pm x} &= \left\{ \frac{(\phi_l)_{i,j}(\phi_l)_{i\pm1,j}}{|(\phi_l)_{i,j}(\phi_l)_{i\pm1,j}|} \right\}, \\ s_{\pm x} &= \min_{l=1,L_{\max}} \{(s_l)_{\pm x}\}, \end{aligned} \tag{10a}$$

where $L_{\max}$ denotes the number of interfaces present in the domain.

The switching function:

$$\chi_{\pm x} = \min_{l=1,L_{\max}} \left\{ |\max((s_l)_{\pm x}, 0)| + \frac{|(\phi_l)_{i,j}|}{\Delta x} |\min((s_l)_{\pm x}, 0)| \right\}. \tag{10b}$$

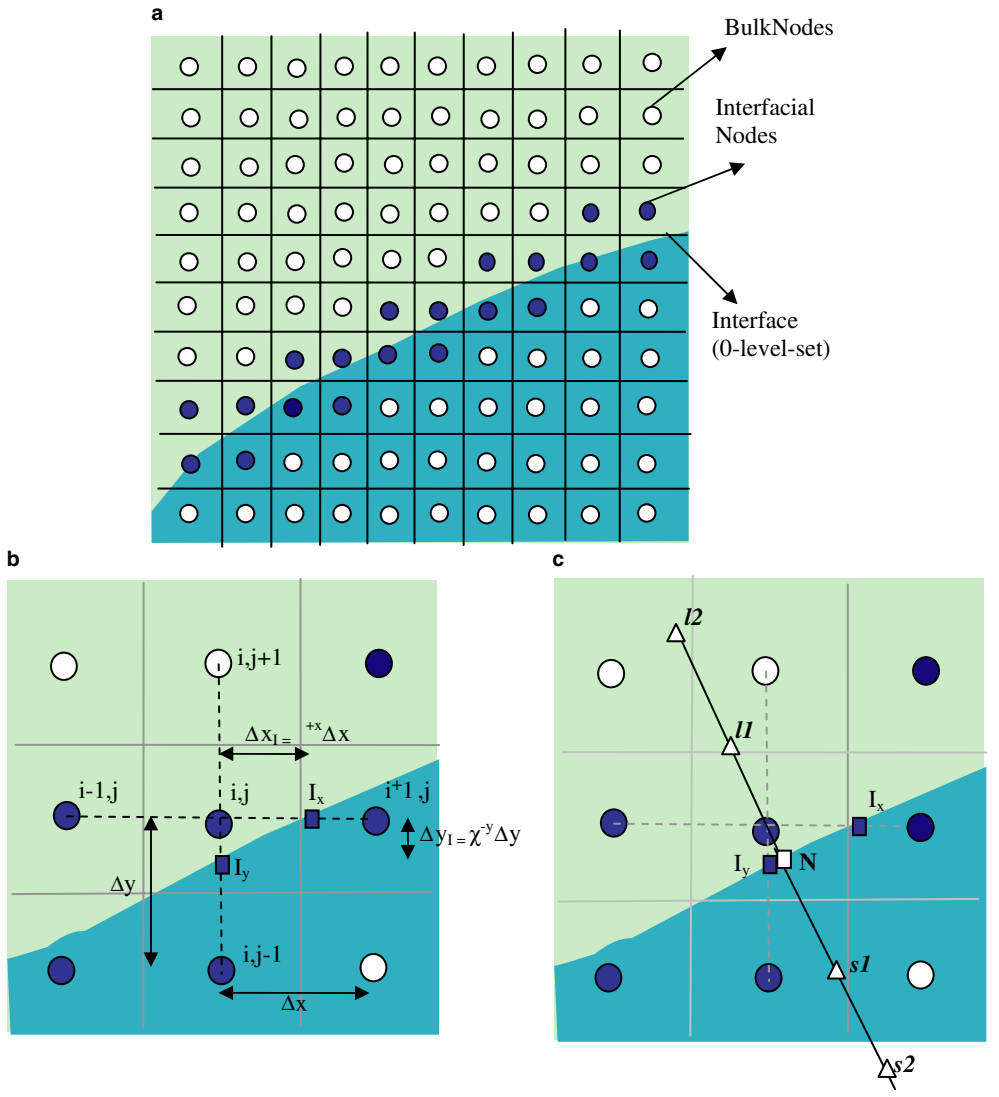

Fig. 1. (a) Definition of the bulk (clear circles) and interfacial (filled circles) nodes. The interface is given by the 0-level-set. (b) The configuration of a typical interfacial node. (c) System for evaluating the normal gradients at the interface.

Then the second derivative w.r.t. x is:

$$\frac{\partial^2\psi}{\partial x^2} = \alpha_{+x}\frac{(\psi_{+x}-\psi_{i,j})}{\gamma_x\Delta x^2} - \alpha_{-x}\frac{(\psi_{i,j}-\psi_{-x})}{\gamma_x\Delta x^2}, \tag{10c}$$

$$\psi_{\pm x} = \psi_{I_{\pm x}}|\min(s_{\pm x},0)| + \psi_{i\pm1,j}|\max(s_{\pm x},0)|, \tag{10d}$$

$$\alpha_{\pm x} = \frac{1}{\chi_{\pm x}}, \tag{10e}$$

$$\gamma_x = \frac{(\chi_{-x}+\chi_{+x})}{2}. \tag{10f}$$

Note that this scheme works for the situations where the point (i,j) lies in the fluid(solid) and either one, none or both of the neighbors $(i+1,j)$ and $(i-1,j)$ lie in the solid(fluid) phase. Also, in constructing the three-dimensional Laplacian operator the coefficients $\alpha_{\pm y}/(\gamma_y \Delta y^2)$ and $\alpha_{\pm z}/(\gamma_z \Delta z^2)$ can be calculated in a manner identical to that $\alpha_{\pm x}/(\gamma_x \Delta x^2)$ for above.

The discrete form of Eqs. (2)–(4) can be constructed using the above operators. The resulting form of the discrete system of equations retains the standard 5-point (7-point) stencil in 2(3)-dimensions. Furthermore, assembly of the discrete equations proceeds in the above algorithm independent of whether the grid point in question is a bulk point (i.e., away from the interface) or an interfacial point (i.e., a point adjacent to the immersed boundary). Thus, the algorithm is simple to implement and in fact a solver operating on a regular Cartesian mesh can be easily modified to deal with moving immersed boundaries using the above formalism. This applies even in the presence of fluid flow [4]. Specification of the interfacial values (such as ψ_{I_x}) in Eq. (10) is the additional piece of information required in the solution of the transport equations.

4.3. Application of interfacial conditions

In the present general treatment of coupled heat and solute transport, several approaches for applying the interface conditions were explored and the following method was deemed to be most suitable, within the framework of an explicit interface update. First, Eqs. (5) and (6) are written in discrete form using the "normal probe" method used in [1].

Thus, for the following general form of the interface conditions (5) and (6):

$$V_N = \left[\beta_S \left(\frac{\partial \psi}{\partial n}\right)_S - \beta_L \left(\frac{\partial \psi}{\partial n}\right)_L\right], \tag{11}$$

where the parameter β depends on whether the temperature field or species field is used to evaluate the interface velocity and is defined specifically later. To calculate the gradient at the interface $\frac{\partial \psi}{\partial n}$ with an $o(\Delta x^2)$ error, we use the values of temperature at two points along the normal probe, as illustrated in Fig. 1(c). Note that the location on the interface from which the normal is projected into the two phases depends on the interface quantity that is to be computed as will be specified below.

In the liquid, the values of the variable ψ at the two points along the normal probe are denoted ψ_{L1} and ψ_{L2}, respectively, and are obtained by bilinear interpolation from the surrounding grid nodes. Let the distance of these two points on the normal probe be dx_{L1} (=Δx, the grid size) and dx_{L2} (=$2\Delta x$), respectively, from the point on the interface where the temperature is to be computed. A Taylor series expansion about the interfacial point gives:

$$\psi_{L1} = \psi_{LI} + \left(\frac{\partial \psi}{\partial n}\right)_L dx_{L1} + \left(\frac{\partial^2 \psi}{\partial n^2}\right)_L \frac{(dx_{L1})^2}{2} + o(dx_{L1}^3), \tag{12}$$

$$\psi_{L2} = \psi_{LI} + \left(\frac{\partial \psi}{\partial n}\right)_L dx_{L2} + \left(\frac{\partial^2 \psi}{\partial n^2}\right)_L \frac{(dx_{L2})^2}{2} + o(dx_{L2}^3). \tag{13}$$

From the above equations, we get the second-order approximation:

$$\left(\frac{\partial \psi}{\partial n}\right)_L = \frac{dx_{L2}^2 \psi_{L1} - dx_{L1}^2 \psi_{L2} - (dx_{L2}^2 - dx_{L1}^2)\psi_{LI}}{dx_{L1} dx_{L2}^2 - dx_{L1}^2 dx_{L2}} \tag{14}$$

which may be written as (since $dx_{L2} = 2dx_{L1}$):

$$\left(\frac{\partial \psi}{\partial n}\right)_L = 2\psi_{L1} - \frac{1}{2}\psi_{L2} - \frac{3}{2}\psi_{LI}. \tag{15}$$

The gradient in the solid can be similarly obtained.

Thus, Eq. (11) becomes:

$$V_{\mathrm{N}} = \left[-\beta_{\mathrm{S}}\left(2\psi_{\mathrm{S1}} - \frac{1}{2}\psi_{\mathrm{S2}} - \frac{3}{2}\psi_{\mathrm{S}I}\right) - \beta_{\mathrm{L}}\left(2\psi_{\mathrm{L1}} - \frac{1}{2}\psi_{\mathrm{L2}} - \frac{3}{2}\psi_{\mathrm{L}I}\right)\right]. \tag{16}$$

4.3.1. Interface conditions for the pure material case

For the pure material case the interface temperature is computed using the Dirichlet condition, Eq. (7), with the species concentrations set to zero. The temperature values are obtained at the locations indicated by the I_x and I_y in Fig. 1(c). These locations are given by:

$$x_{I_x} = x_{i,j} + \Delta x_I, \quad y_{I_x} = y_{i,j}, \tag{17a}$$

$$x_{I_y} = x_{i,j}, \quad y_{I_y} = y_{i,j} - \Delta y_I, \tag{17b}$$

$$\begin{aligned} \frac{\Delta x_I}{\Delta x} &\cong \left|\frac{(\phi_l)_{I_x} - (\phi_l)_{i,j}}{(\phi_l)_{i+1,j} - (\phi_l)_{i,j}}\right| = \left|\frac{0 - (\phi_l)_{i,j}}{(\phi_l)_{i+1,j} - (\phi_l)_{i,j}}\right|, \\ \frac{\Delta y_I}{\Delta y} &\cong \left|\frac{(\phi_l)_{I_y} - (\phi_l)_{i,j}}{(\phi_l)_{i,j} - (\phi_l)_{i,j} - 1}\right| = \left|\frac{0 - (\phi_l)_{i,j}}{(\phi_l)_{i+1,j} - (\phi_l)_{i,j}}\right|. \end{aligned} \tag{17c}$$

Then, for each of the *interfacial points* the interface velocity is computed at the locations denoted by N in Fig. 1(c). The point N is located by:

$$\vec{x}_{\mathrm{N}} = \vec{x}_{i,j} - \vec{n}_{i,j}(\phi_l)_{i,j}, \tag{18}$$

where $\vec{n}_{i,j}$ is the normal at the grid point indexed (i,j). The node points on the normal probe projected from this point into the solid and liquid phases are located at:

$$\vec{x}_{\mathrm{L1}} = \vec{x}_{\mathrm{N}} + \vec{n}_{\mathrm{N}}\,\mathrm{d}x_{\mathrm{L1}}, \tag{19a}$$

$$\vec{x}_{\mathrm{L2}} = \vec{x}_{\mathrm{N}} + \vec{n}_{\mathrm{N}}\,\mathrm{d}x_{\mathrm{L2}}, \tag{19b}$$

$$\vec{x}_{\mathrm{S1}} = \vec{x}_{\mathrm{N}} - \vec{n}_{\mathrm{N}}\,\mathrm{d}x_{\mathrm{S1}}, \tag{19c}$$

$$\vec{x}_{\mathrm{S2}} = \vec{x}_{\mathrm{N}} - \vec{n}_{\mathrm{N}}\,\mathrm{d}x_{\mathrm{S2}}. \tag{19d}$$

Bilinear interpolation is performed from the surrounding mesh points to obtain the value of the required variable ψ to be used in Eq. (16), at the above points $\vec{x}_{\mathrm{L1}}, \vec{x}_{\mathrm{L2}}, \vec{x}_{\mathrm{S1}}, \vec{x}_{\mathrm{S2}}$. The normal vector at N, $\vec{n}_{\mathrm{N}}$ is also obtained by bilinear interpolation from the surrounding mesh points. These are used to compute the interface velocity using Eq. (5) which is discretized using Eq. (16). For the pure material case $\beta_{\mathrm{S}} = St \cdot \frac{k_{\mathrm{S}}}{k_{\mathrm{L}}}$ and $\beta_{\mathrm{L}} = St$.

4.3.2. Interface conditions for the impure material case

The interface velocity is first obtained, for each of the interfacial nodes, using Eq. (9) with the discrete form expressed in Eq. (16). The variable ψ in this case corresponds to the concentration field. For this case $\beta_{\mathrm{S}} = D^*_{\mathrm{L}}\frac{D_{\mathrm{S}}}{D_{\mathrm{L}}(1-k_{\mathrm{p}})c_{\mathrm{L}I}}$ and $\beta_{\mathrm{L}} = D^*_{\mathrm{L}}\frac{1}{(1-k_{\mathrm{p}})c_{\mathrm{L}I}}$. Note that the interface normal velocity is obtained at the interface location marked N. However, this normal velocity is "extended" into the narrow band of the level-set representation [4] and hence the entire narrow band is populated with a level-set velocity field. This level-set velocity field is used to advect the level-sets.

Once the velocity is computed, the interface temperature is obtained using Eq. (5). Using the discrete form in Eq. (16) and the fact that $\Theta_{\mathrm{L}I} = \Theta_{\mathrm{S}I}$, inversion of the equation provides the interface temperature:

$$\Theta_{\mathrm{L}I} = \frac{V_{\mathrm{N}} + \beta_{\mathrm{S}}\left(2\Theta_{\mathrm{S1}} - \frac{1}{2}\Theta_{\mathrm{S2}}\right) + \beta_{\mathrm{L}}\left(2\Theta_{\mathrm{L1}} - \frac{1}{2}\Theta_{\mathrm{L2}}\right)}{\frac{3}{2}(\beta_{\mathrm{S}} + \beta_{\mathrm{L}})}, \tag{20}$$

where $\beta_S = St \cdot \frac{k_S}{k_L}$ and $\beta_L = St$. Note that the value of normal velocity at the point where the interface temperature is to be specified, i.e., at point $I_{x/y}$, is obtained from bilinear interpolation (of the extended velocity field available in the narrow band of the level-set field) from the surrounding grid points. Next, the interface composition on the liquid side of the interface is obtained from Eq. (7) at the points $I_{x/y}$, using the above determined value of the interface temperature. The following nonlinear equation for c_{LI} is solved using a Newton method:

$$b_1 c_{LI} + b_2 c_{LI}^2 + b_3 c_{LI}^3 + b_4 c_{LI}^4 = \Theta_{LI} + \Gamma(\theta)\kappa. \tag{21}$$

The composition on the solid side is then given by the partition coefficient:

$$c_{SI} = k_p c_{LI}. \tag{22}$$

4.4. Overall solution procedure

As described in the previous section, the interfacial conditions in the present case couple the interface position (and curvature), temperature and composition. In previous work [49], due to the explicit interface tracking method used, stable computations of dendritic growth required an implicit approach to couple the boundary update and field equation solver. In the present case, due to the built-in regularization provided by the level-set advection, an explicit approach to time-stepping the interface and temperature and species fields works adequately. The overall solution procedure with boundary motion, for the case of an impure material (the pure material case is specialized below by skipping steps 3, 4, 7, 8 and 9), is as follows:

1. Advance to time $t^{n+1} = t^n + \delta t$.
2. Compute interface temperature for each of the *interfacial* points. This is obtained for impure materials from the interface velocity (obtained at the end of the previous time step) using Eq. (20). This interfacial temperature is obtained at the locations N (Fig. 1(c), Eq. (18)) corresponding to each of the interfacial nodes. For pure materials use Eq. (7).
3. Extend the interface temperatures out (using standard level-set based extension fields as given in [55]) from the interface to populate the narrow band around the zero level-set.
4. Get c_{LI} from Θ_{LI} at each *interfacial* point using Eq. (21). Get c_{SI} from Eq. (22). These interfacial compositions are obtained at locations N (Fig. 1(c), Eq. (18)) for each interfacial point.
5. Using Eq. (16) obtain the interface velocity at locations N for each interfacial point. For pure material ψ is the temperature field while for impure materials it is the composition field. Extend this interfacial velocity into the narrow band of the level-set field.
6. Advance the level-set to its new position.
7. For each interfacial point interpolate the Θ_{LI} previously extended and stored in the narrow band to locations such as I_x and I_y as required. Thereby calculate c_{LI} and c_{SI} using Eqs. (21) and (22).
8. Advance the discretized species equations in time using boundary conditions obtained in step 7.
9. Compute the interface velocity using the newly obtained species field. This repeats steps 4 and 5.
10. Repeat steps 2 and 3. This provides the interfacial temperature conditions for step 11.
11. Compute the temperature field. In order to solve the temperature field the interface temperature value is required at points such as $I_{x/y}$ in interface cells. These values are obtained by bilinear interpolation from the extended interface temperature values Θ_{LI} in the narrow band.
12. Go to step 1 for next time step.

Note that with the above explicit approach stable computations of interface evolution can be performed with time step sizes that are controlled by a CFL-type criterion of the form $\delta t = \lambda \delta x / \max(V_{\text{Interface}})$, where λ is set to 0.1 in the calculations performed.

5. Results

In this section we compute the solidification in the stable and unstable modes for pure as well as impure materials and compare the results of our computations with exact solutions [56], the solvability theory results quoted in [15,28,48,57] and other numerical results [58,59]. The growth and material parameters are varied and the dendritic tip details such as radius, velocity and selection parameter are each compared with theoretical and computational results presented in the above papers.

5.1. The Neumann problem

The stable planar solidification of a circular seed in a pure melt is first simulated to establish order of accuracy of the method. The configuration is shown in Fig. 2(a). The seed is placed at the center of the domain. The Stefan number = 0.1. The exact solution for the Neumann problem is given in [56]. A line heat sink placed at the center of the seed causes it to freeze. The boundary conditions at the edge of the domain and the initial conditions are specified from the exact solution for the problem. The errors in the computed temperature field (Fig. 3(a)) and interface position (Fig. 3(b)) are obtained for different grid sizes and the results are summarized in Fig. 3. For the technique described above, second-order accurate results are obtained. In contrast, if only one point is used in the normal probe technique to extract the interface velocity, the accuracy of the interface position will be first order. This is clearly shown in Fig. 3(c).

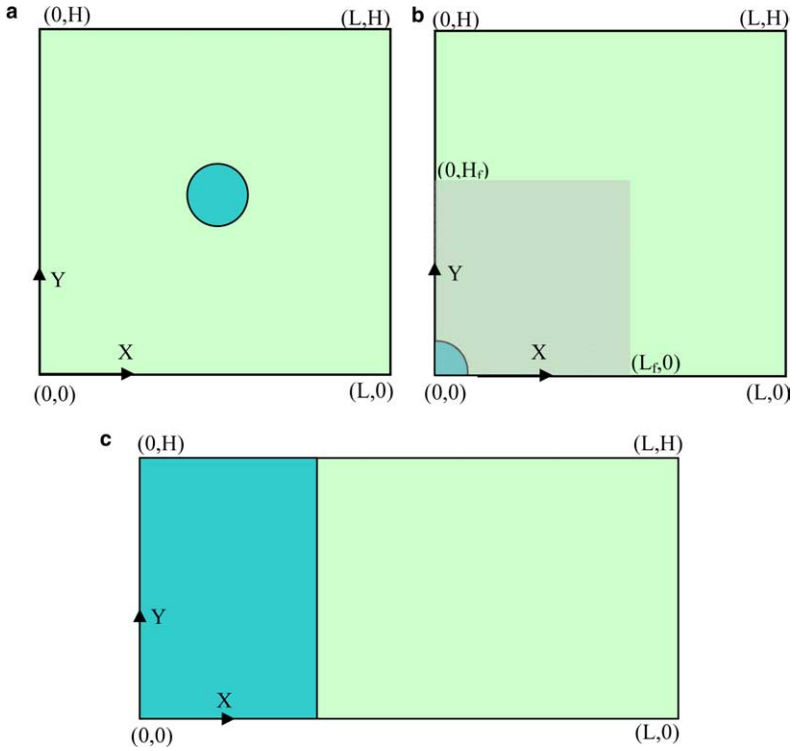

Fig. 2. Computational set-up for: (a) the stable solidification problem and (b) unstable (dendritic) solidification problems. (c) For planar solidification of an aqueous solution.

5.2. Unstable solidification of a pure melt

To establish the accuracy of the approach for simulation of dendritic growth, a seed crystal is placed at the origin in the computational domain shown in Fig. 2(b). The non-dimensionalization in this case is done using a length scale $X = \Gamma_0 = \frac{\gamma_0 T_m \rho C_p}{H_{SL}^2}$, the capillary length, time scale $= \frac{X^2}{\eta_L}$, where $\eta_L = \alpha_L$, temperature scale $T_S = H_{SL}/\rho C_p$. Since a fourfold symmetric crystal is grown, symmetry conditions are applied on the x- and y-axes. The far-field condition corresponds to a non-dimensional undercooling $\Delta = \frac{\rho C_p (T_m - T_\infty)}{H_{SL}} = -0.55$. The radius of the initial seed crystal is 0.075 (5 grid spacings). In the fine mesh zone of extent 2 units shown in Fig. 2(b), 400×400 grid points are employed. Outside of the fine mesh zone a linearly stretched grid is employed consisting of 50 points. In Fig. 4 the results of the dendritic growth calculations are summarized. The figure compares the computed dendritic tip characteristics with those obtained from microscopic solvability theory [28,57]. Three different anisotropy strengths were tested, i.e., $\varepsilon = 0.01, 0.03, 0.05$. The steady-state tip radius ρ_t (Fig. 4(a)), tip velocity V_t (Fig. 4(b)) and tip selection parameter $\sigma^* = \frac{2\alpha_L \gamma_0}{\rho^2 V_t}$ (Fig. 4(c)) show excellent match with the theory.

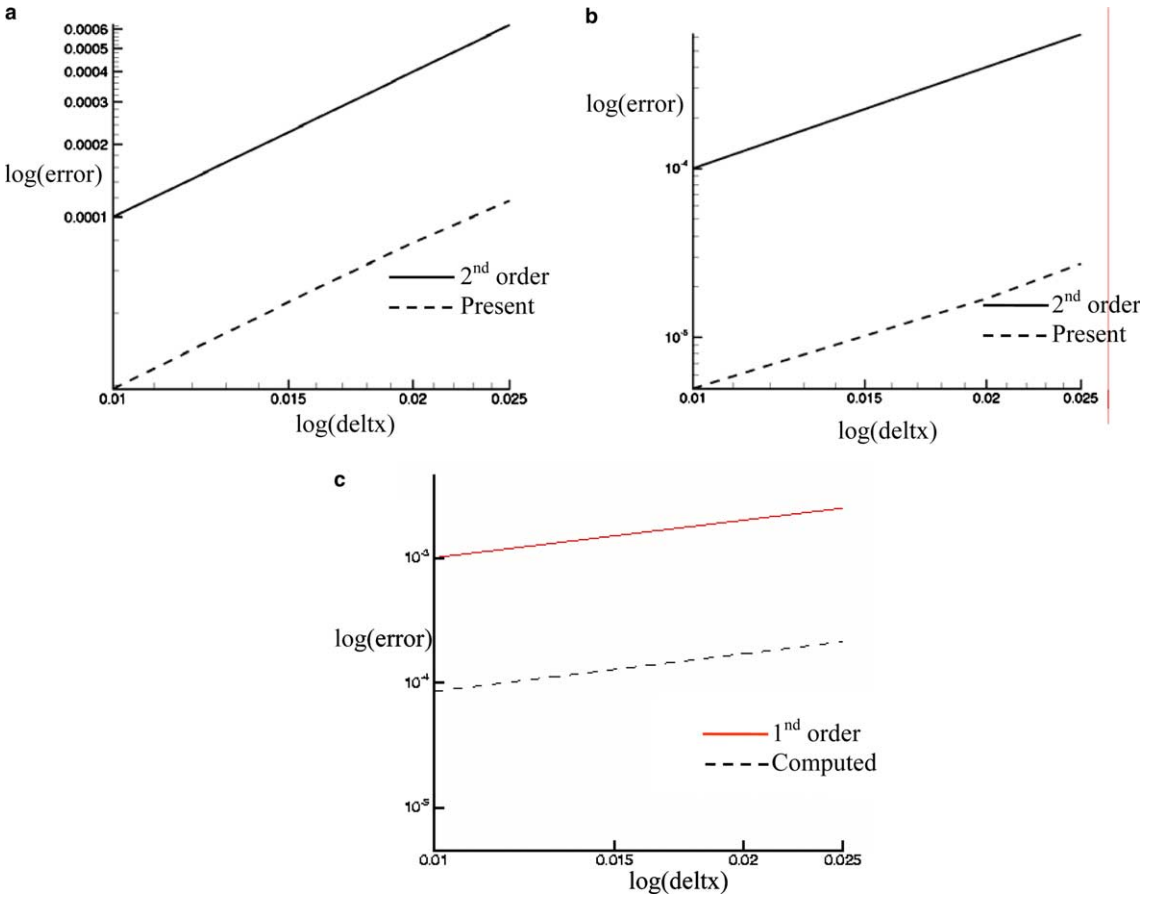

Fig. 3. Error analysis for the Neumann problem: (a) the temperature error against mesh spacing; (b) interface location error against mesh spacing using two probes and (c) interface location error against mesh spacing using one probe.

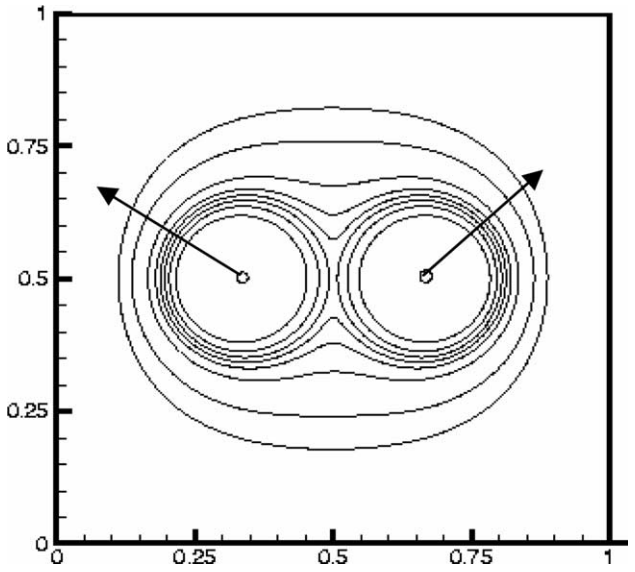

Fig. 4. Growth and merger of two growing circular solid–liquid fronts. The arrow shows the sequence in time.

One advantage of sharp interface methods is that the accuracy of the discretization scheme is evident from the construction of the spatial operators. While designing schemes that provide a desired order of accuracy entail a modest increase in complexity over diffuse interface methods, this added care in constructing the scheme is an advantage from two standpoints: (1) The accuracy of the method can be established explicitly a priori, and (2) since the interface has no thickness the features to be resolved by the grid are related only to the length scales expected to arise from the dynamics of the problem, i.e., the grid needs only to resolve features tangential to the interface. However, typically sharp interface methods have relied on a posteriori convergence analysis to determine if solutions obtained can be considered to be grid independent. It would be useful to take advantage of the predictability of the convergence characteristics of sharp interface methods to provide guidelines as to what mesh sizes will be necessary in order to be confident that the solutions are independent of resolution. In determining this, the relevant length scales to be resolved in a physical problem need to be estimated. In the dendritic growth of pure materials two such length scales can be identified, namely the dendrite tip radius ρ_t and the thermal diffusion length $\delta_t = \frac{\alpha}{V_t}$. Both these quantities can be estimated a priori based on solvability theory. The question is, of course, what is the factor that determines an adequate grid resolution? To explore this, a grid refinement study was performed and the results are collated in Fig. 5. These figures show, for the particular undercooling used ($\Delta = -0.55$) the variation of percentage error of the computed solution with respect to the exact (solvability theory) values of the dendritic tip characteristics plotted for various mesh sizes. The convergence of the results with grid refinement can be seen. Examination of these figures clarifies that the grid spacing Δx_c at convergence is nearly the same for all the anisotropies. In Table 1 the tip radius and the thermal diffusion length (estimated as $\delta_t = \frac{\alpha}{V_t}$) around the tip are quantified for each value of anisotropy. The numbers of grid points necessary to resolve these two length scales are also listed in the table. It can be noted that the number of grid points required to resolve these two length scales for convergence is vastly different for the three different anisotropies indicating that the demand on the grid is not posed by either the need to resolve the tip radius or the thermal diffusion length. In fact, it is apparent that the demands on the grid

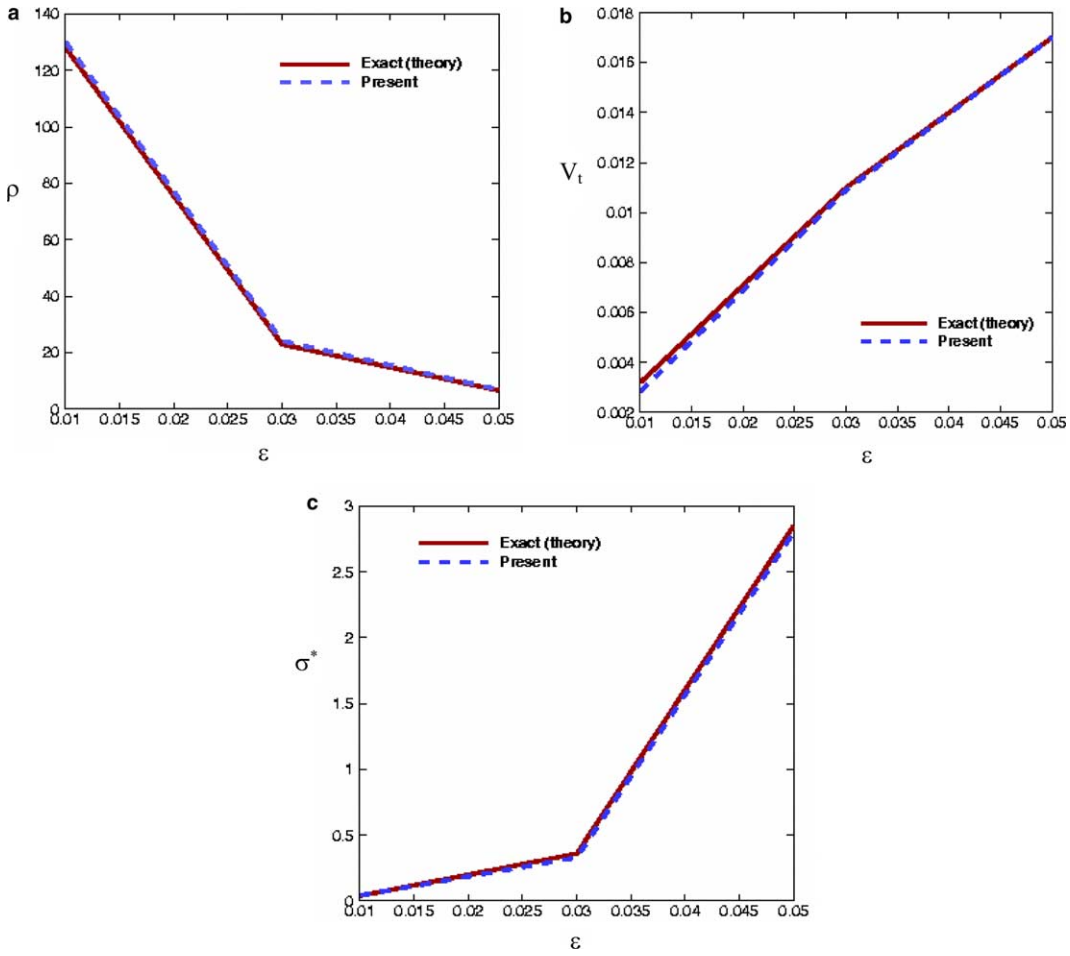

Fig. 5. Comparison of the computed tip characteristics with solvability theory for different anisotropies: (a) dendrite tip radius, (b) dendrite tip velocity, (c) tip selection parameter.

Table 1
Comparison of the grid spacing necessary to obtain grid independent solutions for different anisotropies

ε	ρ_t	δ_t	$\frac{\delta_t}{\Delta x_c}$	$\frac{\rho_t}{\Delta x_c}$
0.05	0.0176	0.147	44.05	5.3
0.03	6.13e − 2	0.229	68.96	18.38
0.01	0.323	0.874	262.47	97.08

are nearly independent of the tip characteristics and nearly the same for all three cases. In fact Δx_c value corresponds to approximately 2 Γ_0 where $\Gamma_0 = \frac{\gamma_0 T_m \rho C_p}{H_{SL}^2}$ is a capillary length. Physically, at least for the fairly large undercoolings considered here, it appears that this capillary length needs to be resolved by the grid in order to obtain grid independent results. Based on this notion, it is straightforward to pick the mesh size that provides grid independent solutions for sharp interface calculations. This estimate is useful both for selecting a suitable uniform mesh as well to establish criteria for locally refined meshes in the vicinity of the dendrite surfaces.

5.3. Planar (1D) solidification of an aqueous salt solution

We compute the solidification of a sample containing an aqueous salt solution in the setup shown in Fig. 2(c). Such a system occurs commonly in the cryopreservation of biological materials (cells and tissue). This one-dimensional case was solved using a moving coordinate system fixed at the advancing front by [58]. Numerical (finite-difference) solutions were obtained for the temperature and solute fields ahead of the front. The parameters employed in the present calculations are the same as those of [54]:

$$c_0 = 0.1548\ \text{mol l}^{-1}, \quad \alpha_L = 0.115\ \text{mm}^2\ \text{s}^{-1}, \quad \alpha_S = 1.364\ \text{mm}^2\ \text{s}^{-1}, \quad D_L = 7.8 \times 10^{-4}\ \text{mm}^2\ \text{s}^{-1},$$

$$D_S = 7.8 \times 10^{-7}\ \text{mm}^2\ \text{s}^{-1}, \quad H_{SL} = 0.333\ \text{J mm}^{-3}, \quad T_m = 273.15\ \text{K}, \quad k = \frac{(c_{LI})_S}{(c_{LI})_L} = 1.00 \times 10^{-3},$$

$$k_L = 5.36 \times 10^{-4}\ \text{J mm}^{-1}\ \text{s}^{-1}\ \text{K}^{-1}, \quad k_S = 2.34 \times 10^{-3}\ \text{J mm}^{-1}\ \text{s}^{-1}\ \text{K}^{-1}.$$

The phase diagram is represented by the relationship:

$$T_{LI} = b_0 + b_1 c_{LI} + b_2 c_{LI}^2 + b_3 c_{LI}^3 + b_4 c_{LI}^4,$$

where:

$$b_0 = 273.15\ \text{K}, \quad b_1 = -3.362\ \text{K l mol}^{-1}, \quad b_2 = -0.0414\ \text{K l}^2\ \text{mol}^{-2},$$
$$b_3 = -0.0404\ \text{K l}^3\ \text{mol}^{-3}, \quad b_4 = -6.616 \times 10^{-4}\ \text{K l}^4\ \text{mol}^{-4}.$$

The non-dimensionalization in this case uses length scale $X = 1$ mm, time scale $= \frac{X^2}{\eta_L}$, where $\eta_L = D_L$, temperature scale $T_S = b_0$, concentration scale=c_0. The temperature at the left boundary in Fig. 2(c) (on the solid) is decreased in time at a specified constant (non-dimensional) cooling rate B. The range of cooling rates investigated in the following is typical of the rates employed in cryo-protocols [60–62]. The right wall is treated as an adiabatic boundary. The solid–liquid front then advances in the $+x$ direction.

A typical case is shown in Figs. 6(a) and (b). The cooling rate in Fig. 6(a) is $B = -0.05$. This is the lowest cooling rate computed. Fig. 6(a) shows the temperature field at various instants of time as the front advances to the right. As can be seen, at this low cooling rate, the temperature field has only mild variations in space due to the large thermal diffusivity. However, as shown in Fig. 6(b) the solute is segregated into the solution as the ice forms and a solute boundary layer progressively accumulates ahead of the front. The solute layer steepens as time progresses since almost pure ice forms upon solidification. For this growth configuration there is a region of constitutionally supercooled solution in front of the ice-liquid boundary. The results shown in Figs. 6(a) and (b) are in excellent agreement with those in [58,59]. It is to be noted that the present sharp interface method captures the solute buildup on the liquid side of the interface as a discontinuity and also treats the diffusivity jump between the solid and liquid as a jump discontinuity. Thus, in the calculations performed here, the salt is rejected into the remaining solution entirely while nearly pure solid (ice) forms.

The interface location for various cooling rates (highest value of -1 K/s to lowest value of -0.05 K/s) is plotted against time in Fig. 6(c). These curves were produced to compare with identical curves in [58,59]. In Fig. 6(c), the solid lines are curves obtained by the present method, while the dotted lines are those in [58]. There is close agreement between the results.

5.4. Dendritic solidification of a binary solution

The dendritic growth of crystals with the coupled transport of heat and solute is computed for a range of physical parameters. These cases are designed to demonstrate the capability of the present sharp interface

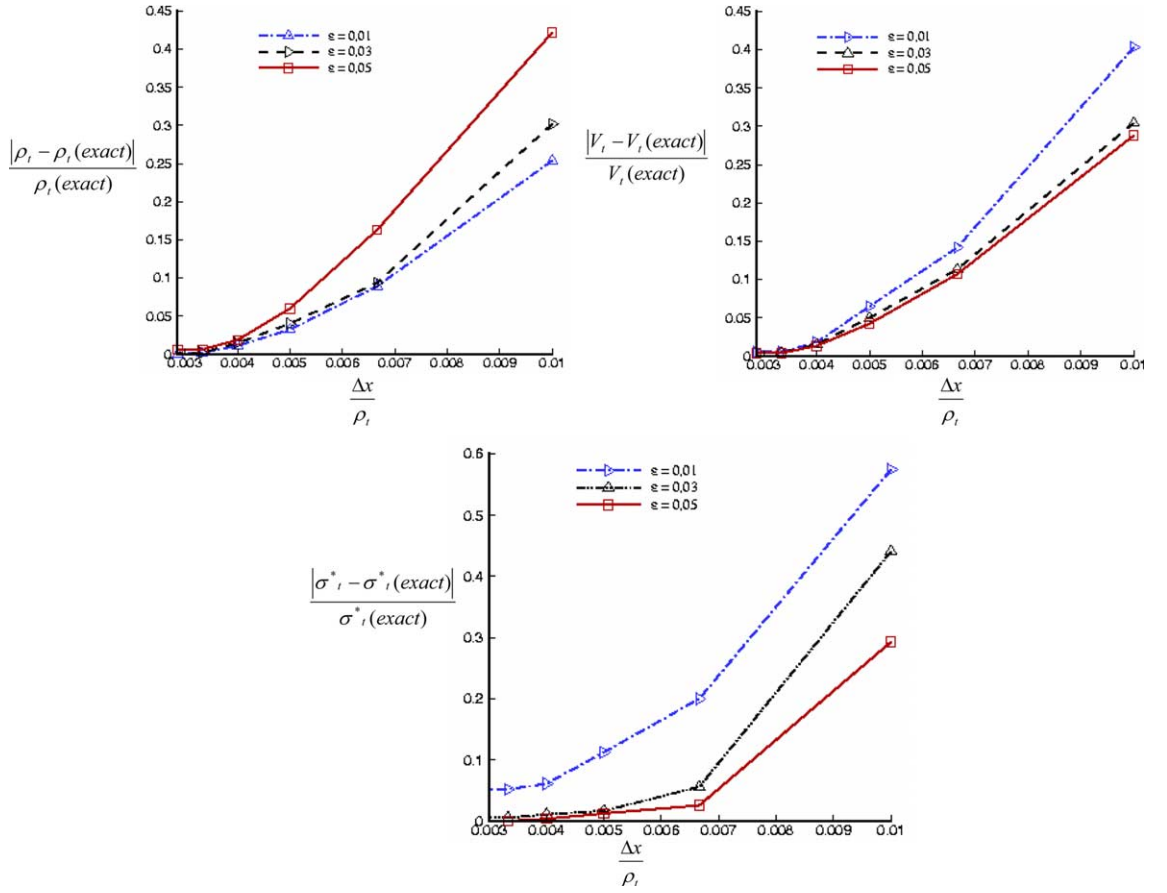

Fig. 6. Percentage error (with respect to the solvability theory values) in computing the tip properties plotted against the grid spacing employed. (a) Tip radius error, (b) tip velocity error, and (c) tip selection parameter error.

technique to compute the large distortions of the phase boundary, while maintaining discontinuities in the material properties and solute fields across the boundary. Here we show that the results display the correct physically expected trends as the growth parameters are varied.

Fig. 7 shows the evolution of shapes of dendrites grown in a melt (in the domain shown in Fig. 2(b), with the same non-dimensionalization as in Section 4.3) where the boundaries of the melt away from the seed crystal are cooled with a constant cooling rate $B = -0.1$. The anisotropy strengths are varied to produce the dendritic shapes shown in Figs. 7(a) ($\varepsilon = 0.01$), 7(b) ($\varepsilon = 0.03$) and Figs. 7(c) ($\varepsilon = 0.05$). The shapes of the dendrites for each case display the physically correct qualitative behavior, with the lowest anisotropy dendrite showing weak tip selection. This dendrite appears to experience a tip-splitting mode of breakdown in the later stages of growth. The highly corrugated interface is handled well by the sharp interface approach. The low anisotropy case appears to lose tip stability and similar to the pure material case (see discussion in Section 5.2) the grid-induced noise affects the evolution of this weakly stabilized tip. In Figs. 7(d)–(f) are displayed the solute fields surrounding the tip for the final shapes shown in Figs. 7(a)–(c), respectively. The microsegregation of solute in the grooves between the dendritic arms are clearly seen in the figure. In the sharp interface method these microsegregation patterns are clearly established because the interface is not smeared. This can be gathered from the lack

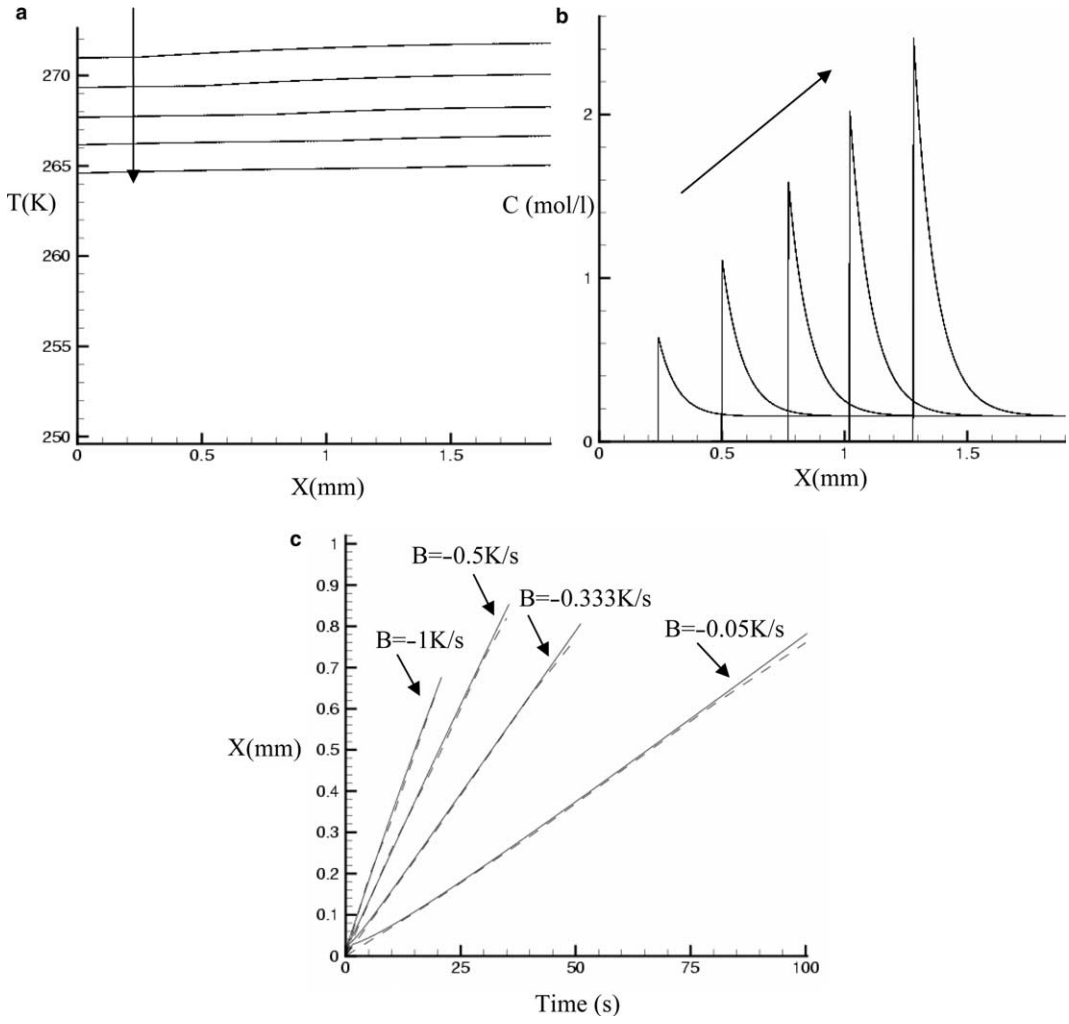

Fig. 7. 1D solidification of an aqueous solution. (a) Temperature field in the liquid and solid phases for a cooling rate of $B = -0.05$ K/s plotted at time intervals of 40 s. The arrow indicates the time sequence. (b) Species concentrations in the solid and liquid phases at the same time instants. (c) Plot of interface position against time for different cooling rates. The dotted line is the trajectory computed from the present approach and the full line is that from Koerber et al.

of contours of solute in the nearly pure solid. Fig. 8 shows the dendritic shapes obtained for cooling rates an order of magnitude apart. The significant differences in the solute gradients in the boundary layer (due to the faster growth velocity of the dendrite in Fig. 8(b)) and microsegregation are illustrated in this figure. Finally, to establish that the grid anisotropy had no effect on the dendrite tip characteristics, in Fig. 9 the dendrite was grown with an orientation (provided by the factor θ_0 in Eq. (8)) of 45° with respect to the mesh. The shape of the tip was compared with a dendrite oriented such that the growth directions were along the Cartesian directions, as shown in Fig. 7(c). The dendrites obtained were found to be independent of grid anisotropy for the primary stem. The less well-resolved secondary arms showed minor influences of the misorientation (Fig. 10).

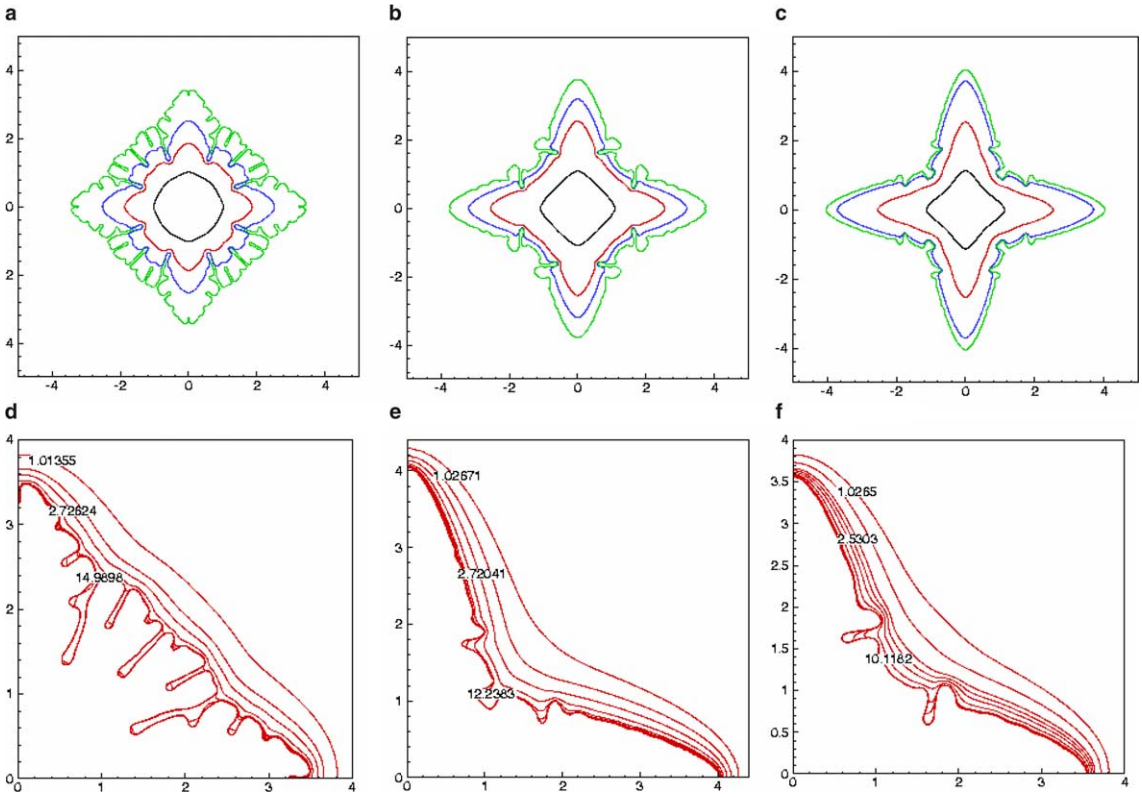

Fig. 8. Dendrite shape evolution for $\sigma = 0.0001$, $\beta = -0.1$ and (a) $\varepsilon = 0.01$, (b) $\varepsilon = 0.03$, (c) $\varepsilon = 0.05$. (d)–(f) Species concentration fields at the final shape corresponding to (a)–(c), respectively.

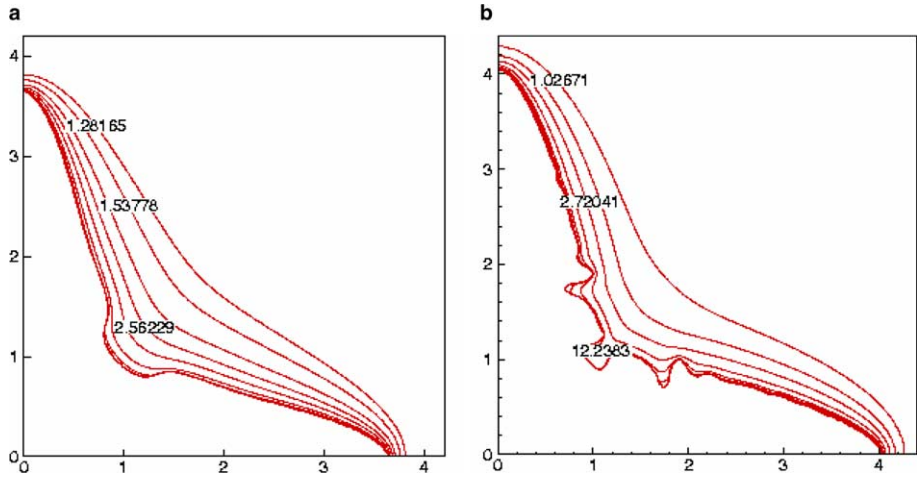

Fig. 9. Dendrite shapes for different cooling rates with $\sigma = 0.0001$, $\varepsilon = 0.05$ (a) $B = -0.01$, (b) $B = -0.1$.

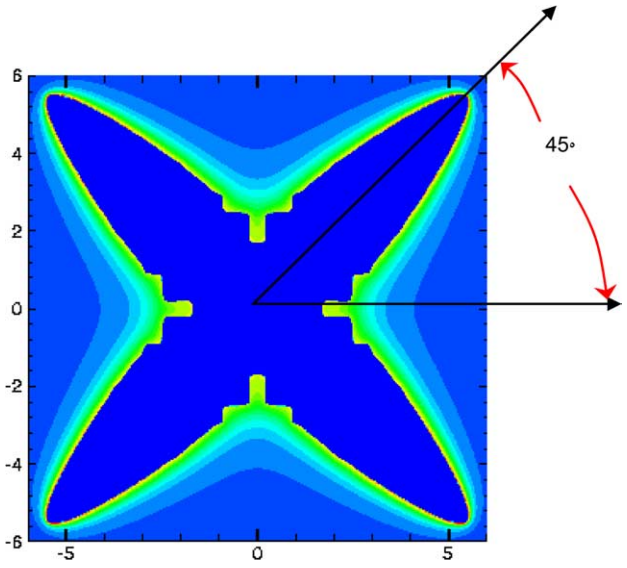

Fig. 10. Dendrite shape for demonstration of grid independence with $\sigma = 0.0001$, $\varepsilon = 0.05$, $B = -0.01$.

6. Summary

A sharp-interface technique for the evolution of phase boundaries on fixed Cartesian meshes is developed and validated. The central point of the paper is that the framework adopted here enables sharp-interface dendritic growth calculations, for pure as well as impure materials, and the formulation and implementation of the method is very simple. In terms of the solution of the heat and solute transport equations, the discretization in the presence of sharp interfaces entails only a few additional lines of code when compared to a straightforward Cartesian grid diffusion solver with no interfaces. Extension to three-dimensions should present no difficulties. Extreme interface contortions including topological changes can be handled easily due to the level-set tracking procedure. The issues underlying second-order accurate interface advection have been addressed in this work. The results for both pure and impure materials demonstrate that the method produces accurate solidification simulations.

Acknowledgments

This work was supported in part by a National Science Foundation CAREER Award (CTS-0092750) and a Whitaker Foundation Biomedical Engineering Research Grant to the second author.

References

[1] H.S. Udaykumar, R. Mittal, W. Shyy, Computation of solid–liquid phase fronts in the sharp interface limit on fixed grids, J. Comput. Phys. 153 (2) (1999) 535–574.
[2] H.S. Udaykumar, R. Mittal, P. Rampunggoon, Interface tracking finite volume method for complex solid–fluid interactions on fixed meshes, Commun. Numer. Meth. Eng. 18 (2) (2002) 89–97.
[3] T. Ye, R. Mittal, H.S. Udaykumar, W. Shyy, An accurate Cartesian grid method for viscous incompressible flows with complex immersed boundaries, J. Comput. Phys. 156 (2) (1999) 209–240.

[4] S. Marella, S. Krishnan, H. Liu, H.S. Udaykumar, Sharp interface cartesian grid method I: an easily implemented technique for 3D moving boundary computations, J. Comput. Phys. 209 (2) (2005), in press.
[5] X.D. Liu, R.P. Fedkiw, M.J. Kang, A boundary condition capturing method for Poisson's equation on irregular domains, J. Comput. Phys. 160 (1) (2000) 151–178.
[6] R. Leveque, J. Zhilin Li, The immersed interface method for elliptic equations with discontinous coefficients and singular sources, SIAM J. Numer. Anal. 31 (4) (1994) 1019–1044.
[7] Z.L. Li, M.C. Lai, The immersed interface method for the Navier–Stokes equations with singular forces, J. Comput. Phys. 171 (2) (2001) 822–842.
[8] D.M. Anderson, G.B. McFadden, A.A. Wheeler, A phase-field model of solidification with convection, Physica D 135 (1-2) (2000) 175–194.
[9] C. Beckermann, H.J. Diepers, I. Steinbach, A. Karma, X. Tong, Modeling melt convection in phase-field simulations of solidification, J. Comput. Phys. 154 (2) (1999) 468–496.
[10] W.J. Boettinger, S.R. Coriell, A.L. Greer, A. Karma, W. Kurz, M. Rappaz, R. Trivedi, Solidification microstructures: recent developments, future directions, Acta Mater. 48 (1) (2000) 43–70.
[11] L.Q. Chen, Phase-field models for microstructure evolution, Annu. Rev. Mater. Res. 32 (2002) 113–140.
[12] S. Chen, B. Merriman, S. Osher, P. Smereka, A simple level set method for solving Stefan problems, J. Comput. Phys. 135 (1) (1997) 8–29.
[13] F. Gibou, R. Fedkiw, R. Caflisch, S. Osher, A level set approach for the numerical simulation of dendritic growth, SIAM J. Sci. Comput. 19 (1–3) (2003) 183–199.
[14] T.Y. Hou, Z.L. Li, S. Osher, H.K. Zhao, A hybrid method for moving interface problems with application to the Hele–Shaw flow, J. Comput. Phys. 134 (2) (1997) 236–252.
[15] Y.T. Kim, N. Goldenfeld, J. Dantzig, Computation of dendritic microstructures using a level set method, Phys. Rev. E 62 (2) (2000) 2471–2474.
[16] A. Jacot, M. Rappaz, A pseudo-front tracking technique for the modelling of solidification microstructures in multi-component alloys, Acta Mater. 50 (8) (2002) 1909–1926.
[17] A. Schmidt, Computation of three dimensional dendrites with finite elements, J. Comput. Phys. 125 (2) (1996) 293–312.
[18] P. Zhao, J.C. Heinrich, Front-tracking finite element method for dendritic solidification, J. Comput. Phys. 173 (2) (2001) 765–796.
[19] P. Zhao, M. Venere, J.C. Heinrich, D.R. Poirier, Modeling dendritic growth of a binary alloy, J. Comput. Phys. 188 (2) (2003) 434–461.
[20] N. Al-Rawahi, G. Tryggvason, Numerical simulation of dendritic solidification with convection: two-dimensional geometry, J. Comput. Phys. 180 (2) (2002) 471–496.
[21] N. Al-Rawahi, G. Tryggvason, Numerical simulation of dendritic solidification with convection: three-dimensional flow, J. Comput. Phys. 194 (2) (2004) 677–696.
[22] D. Juric, G. Tryggvason, A front-tracking method for dendritic solidification, J. Comput. Phys. 123 (1) (1996) 127–148.
[23] M. Rappaz, J.L. Desbiolles, C.A. Gandin, S. Henry, A. Semoroz, P. Thevoz, Modelling of solidification microstructures, Solidification Gravity 2000 329-3 (2000) 389–396.
[24] M.F. Zhu, C.P. Hong, A three dimensional modified cellular automaton model for the prediction of solidification microstructures, Isij Int. 42 (5) (2002) 520–526.
[25] D.M. Anderson, G.B. McFadden, A.A. Wheeler, Diffuse-interface methods in fluid mechanics, Annu. Rev. Fluid Mech. 30 (1998) 139–165.
[26] A. Karma, Phase-field formulation for quantitative modeling of alloy solidification, Phys. Rev. Lett. 8711 (11) (2001).
[27] A. Karma, Y.H. Lee, M. Plapp, Three-dimensional dendrite-tip morphology at low undercooling, Phys. Rev. E 61 (4) (2000) 3996–4006.
[28] A. Karma, W.J. Rappel, Quantitative phase-field modeling of dendritic growth in two and three dimensions, Phys. Rev. E 57 (4) (1998) 4323–4349.
[29] D.A. Kessler, J. Koplik, H. Levine, Pattern selection in fingered growth phenomena, Adv. Phys. 37 (3) (1988) 255–339.
[30] J.S. Kirkaldy, Spontaneous evolution of spatiotemporal patterns in materials, Rep. Prog. Phys. 55 (6) (1992) 723–795.
[31] E. Burman, A. Jacot, M. Picasso, Adaptive finite elements with high aspect ratio for the computation of coalescence using a phase-field model, J. Comput. Phys. 195 (1) (2004) 153–174.
[32] K. Glasner, Nonlinear preconditioning for diffuse interfaces, J. Comput. Phys. 174 (2) (2001) 695–711.
[33] C.W. Lan, Y.C. Chang, Efficient adaptive phase field simulation of directional solidification of a binary alloy, J. Cryst. Growth 250 (3–4) (2003) 525–537.
[34] M. Plapp, A. Karma, Multiscale finite-difference-diffusion Monte-Carlo method for simulating dendritic solidification, J. Comput. Phys. 165 (2) (2000) 592–619.
[35] N. Provatas, N. Goldenfeld, J. Dantzig, Adaptive mesh refinement computation of solidification microstructures using dynamic data structures, J. Comput. Phys. 148 (1) (1999) 265–290.
[36] C.S. Peskin, Numerical analysis of blood flow in the heart, J. Comput. Phys. 25 (220–243) (1977).

[37] M.C. Lai, Z.L. Li, A remark on jump conditions for the three-dimensional Navier–Stokes equations involving an immersed moving membrane, Appl. Math. Lett. 14 (2) (2001) 149–154.
[38] R.J. Leveque, Z.L. Li, The immersed interface method for elliptic-equations with discontinuous coefficients and singular sources (vol. 31, p. 1019, 1994), SIAM J. Numer. Anal. 32 (5) (1995) 1704–1704.
[39] H.S. Udaykumar, S. Marella, S. Krishnan, Sharp-interface simulation of dendritic growth with convection: benchmarks, Int. J. Heat Mass Transfer 46 (14) (2003) 2615–2627.
[40] H.S. Udaykumar, R. Mittal, P. Rampunggoon, A. Khanna, A sharp interface Cartesian grid method for simulating flows with complex moving boundaries, J. Comput. Phys. 174 (1) (2001) 345–380.
[41] R.P. Fedkiw, T. Aslam, B. Merriman, S. Osher, A non-oscillatory Eulerian approach to interfaces in multimaterial flows (the ghost fluid method), J. Comput. Phys. 152 (2) (1999) 457–492.
[42] J. Chessa, T. Belytschko, An extended finite element method for two-phase fluids, J. Appl. Mech. – Trans. ASME 70 (1) (2003) 10–17.
[43] J. Chessa, P. Smolinski, T. Belytschko, The extended finite element method (XFEM) for solidification problems, Int. J. Numer. Meth. Eng. 53 (8) (2002) 1959–1977.
[44] J. Dolbow, N. Moes, T. Belytschko, An extended finite element method for modeling crack growth with frictional contact, Comput. Method Appl. Mech. 190 (51–52) (2001) 6825–6846.
[45] N. Sukumar, D.L. Chopp, N. Moes, T. Belytschko, Modeling holes and inclusions by level sets in the extended finite-element method, Comput. Method Appl. Mech. 190 (46–47) (2001) 6183–6200.
[46] F. Gibou, R.P. Fedkiw, L.T. Cheng, M.J. Kang, A second-order-accurate symmetric discretization of the Poisson equation on irregular domains, J. Comput. Phys. 176 (1) (2002) 205–227.
[47] M. Jaeger, M. Carin, The front-tracking ALE method: application to a model of the freezing of cell suspensions, J. Comput. Phys. 179 (2) (2002) 704–735.
[48] H.S. Udaykumar, L. Mao, R. Mittal, A finite-volume sharp interface scheme for dendritic growth simulations: comparison with microscopic solvability theory, Numer. Heat Transfer B 42 (5) (2002) 389–409.
[49] H.S. Udaykumar, L. Mao, Sharp-interface simulation of dendritic solidification of solutions, Int. J. Heat Mass Transfer 45 (24) (2002) 4793–4808.
[50] L. Mao, H.S. Udaykumar, J.O.M. Karlsson, Simulation of micro-scale interaction between ice and biological cells, Int. J. Heat Mass Transfer 46 (26) (2003) 5123–5136.
[51] J.W. Garvin, H.S. Udaykumar, Particle-solidification front dynamics using a fully coupled approach, Part 1: methodology, J. Cryst. Growth 252 (1–3) (2003) 451–466.
[52] J.W. Garvin, H.S. Udaykumar, Particle-solidification front dynamics using a fully coupled approach, part II: comparison of drag expressions, J. Cryst. Growth 252 (1–3) (2003) 467–479.
[53] H. Liu, S. Krishnan, S. Marella, H.S. Udaykumar, Sharp interface Cartesian grid method II: a technique for simulating droplet impact on surfaces of arbitrary shape. J. Comput. Phys. (to appear).
[54] C. Korber, M.W. Schiewe, K. Wollhover, Solute polarization during planar freezing of aqueous salt solutions, Int. J. Heat Mass Transfer 26 (8) (1983) 1241–1253.
[55] J.A. Sethian, P. Smereka, Level set methods for fluid interfaces, Annu. Rev. Fluid Mech. 35 (2003) 341–372.
[56] H.S. Carslaw, J.C. Jaeger, Conduction of Heat in Solids, Oxford University Press, Oxford, 1959.
[57] X. Tong, C. Beckermann, A. Karma, Velocity and shape selection of dendritic crystals in a forced flow, Phys. Rev. E 61 (1) (2000) R49–R52.
[58] K. Wollhover, C. Korber, M.W. Scheiwe, U. Hartmann, Unidirectional freezing of binary aqueous-solutions – an analysis of transient diffusion of heat and mass, Int. J. Heat Mass Transfer 28 (4) (1985) 761–769.
[59] C.V. Studholme, Modeling heat and mass transport in biological tissues during freezing, MS Thesis, University of Alberta, Edmonton, Alta., 1997.
[60] B. Rubinsky, M. Ikeda, A cryomicroscope using directional solidification for the controlled freezing of biological-material, Cryobiology 22 (1) (1985) 55–68.
[61] J.O.M. Karlsson, E.G. Cravalho, M. Toner, A model of diffusion-limited ice growth inside biological cells during freezing, J. Appl. Phys. 75 (9) (1994) 4442–4445.
[62] J.O.M. Karlsson, A. Eroglu, T.L. Toth, E.G. Cravalho, M. Toner, Fertilization and development of mouse oocytes cryopreserved using a theoretically optimized protocol, Human Reproduction 11 (6) (1996) 1296–1305.